Hindawi
Scientific Programming
Volume 2022, Article ID 3091679, 9 pages
https://doi.org/10.1155/2022/3091679

Research Article

MRI Images Based on Semiautomatic Segmentation Algorithm for Prediction of Histological Grade of Breast Tumor

Jiyuan Wang,[1] **Yanling Zhou**,[2] **Shaokun Sun**,[2] **Wenqian Xu**,[2] **and Hanqing Zou**[2]

[1]*General Surgery Block-9A, Suzhou Kowloon Hospital, Shanghai Jiaotong University School of Medicine, Suzhou 215028, China*
[2]*Department of General Surgery, the Second Affiliated Hospital of Soochow University, Suzhou 215004, China*

Correspondence should be addressed to Hanqing Zou; 189040061@stu.just.edu.cn

Received 20 September 2021; Revised 31 January 2022; Accepted 3 February 2022; Published 3 March 2022

Academic Editor: M Pallikonda Rajasekaran

This study aimed to explore the effects of delayed enhanced magnetic resonance imaging (MRI) (DE-MRI) image features based on the semiautomatic circle-dependent (SCD)-based multiphase level set (MLS) (SCD-MLS) algorithm in predicting the histological grade of breast tumors. We explore the clinical effect of DE-MRI on the prediction of the histological grade of breast tumors (BTs). In this study, 264 breast tumor (BT) patients from The Second Affiliated Hospital of Soochow University were selected as the research objects, and DE-MRI examinations were performed. The SCD-MLS algorithm was compared with the Live-Wire algorithm for the segmentation effect and was applied to the DE-MRI image for prediction of the histological grade of BT. The results proved that the SCD-MLS algorithm in this study showed a more accurate segmentation effect with good stability. BT tissue showed a patchy low signal on T1WI and a high signal on T2WI. The number of patients with grade II was the highest ($P < 0.05$); the lesion diameters of grade II and grade III were concentrated at 1.5–2.5 cm and 2.5–3.5 cm, respectively ($P < 0.05$); the fractional anisotropy (FA) of patients with grade I was the largest ($P < 0.05$); and the apparent diffusion coefficient (ADC) of the patients with grade III was the highest ($P < 0.05$). In short, DE-MRI showed a good performance in the BT diagnosis, and the grading of BT tissue was related to lesion size, number of lesions, ADC, and FA.

1. Introduction

Breast tumors (BTs) are caused by genetic mutations in breast glandular epithelial cells under the combined action of a variety of carcinogens [1]. The incidence of BT is increasing year by year, which is a serious threat to women's physical and mental health as well as quality of life [2]. BT has become a major public health topic in the current society, but its etiology is not yet fully understood. Studies have found that there is a certain regularity in the onset of BT and women with high-risk factors for BT are prone to BT [3].

Magnetic resonance imaging (MRI) is a kind of imaging examination of the internal organs of the human body using a magnetic field and a silent electric wave energy pulse. It uses the principle of nuclear magnetic resonance to draw the internal structure image of the object [4]. It is widely used in clinical practice for preoperative pathological classification of BT histology. Compared with conventional ultrasound, CT, and other imaging evaluations, MRI has more practical significance in preoperative evaluation of the therapeutic effect of BT and the determination of lesions [5]. Among them, delayed enhanced magnetic resonance imaging (DE-MRI) has become the main means of examining BT [6, 7]. The image sequence of scanning imaging can clearly observe the imaging characteristics of the tumor, determine the location of the lesion, and evaluate the lesion size and shape [8]. In clinical research, DE-MRI images of BT are segmented mainly by manual delineation, which requires physicians to have a very professional level and years of work experience and requires a large amount of data input, which is time-consuming. In addition, the segmentation results of different physicians or the same physician at different time periods will also be different, which requires a new study [9]. Therefore, this study innovatively used the SCD-MLS algorithm to segment, identify, and analyze MRI images to overcome the shortcomings of manual processing, such as

laborious process and large errors. The study of DE-MRI based on a computer semiautomatic segmentation algorithm for BT tissue classification has very important clinical guiding significance. Semiautomatic segmentation algorithms are mainly divided into energy minimum algorithms, threshold-based segmentation algorithms, and feature-based clustering algorithms [10]. In terms of the accuracy of segmentation alone, the threshold-based algorithms and feature-based clustering algorithms are still insufficient to support the current system requirements. The energy minimum algorithm can not only avoid the influence of noise but also directly integrate the existing knowledge data with the segmentation system, and its scalability is extremely prominent. The level set is one of the representatives of the energy minimum algorithm, which converts the curve in the space into a level set using a higher-level function so that the minimum value of the objective function converges near the target area [11]. Based on the gray distribution characteristics of DE-MRI images for BT, the semiautomatic circle-dependent-based multiphase level set (SCD-MLS) algorithm was proposed in this study [12], which can not only solve the blurred BT boundaries but also combine MLS with circular penalty items to better show the tumor distribution area.

The CSD-MLS algorithm was compared with the Live-Wire algorithm in terms of Dice coefficient and was applied to the MRI images of 264 patients with BT to grade the BT tissues. The lesion diameter, number of lesions, FA value, and ADC value of patients with different historical grades were compared in detail, so as to use the DE-MRI image based on SCD-MLS to evaluate the relationship between the lesion diameter, lesion number, FA value, and ADC value and patients with different historical grades and analyze the evaluation effect of the DE-MRI image.

2. Materials and Methods

2.1. Research Samples. Two hundred sixty-four patients with BT who were admitted to the hospital from January 2017 to May 2020 were selected as the research objects, with an age range of 2475 years, including 14 males and 250 females. There is a total of 293 lesions, including 184 single lesions, 97 double lesions, and 12 triple lesions. The study had been approved by the ethics committee of the hospital, and the patients and their families had understood the study and signed the informed consent forms.

The inclusion criteria were defined as follows: patients who had not received surgical treatment; patients without contraindications to MRI scanning; and patients with clear consciousness and normal examination.

The exclusion criteria were defined as follows: patients with other malignant tumors; patients with mental illness; patients with incomplete clinical data and imaging data; and patients who withdrew from the study due to their own reasons.

2.2. DE-MRI. The 64-slice spiral MRI scanner was adopted for MRI examination in this study. Before scanning, the patient was required to be told about the examination process and precautions to keep the patient in a stable state of mind and breathing. After the contrast agent was injected, there was a short-term thermal response, which should not result in posture changes. During the scanning, the patient was placed in the prone position, the bilateral breasts were perpendicular to the breast circle, and the conventional sagittal, transverse, and coronal scans were performed in turn. The plain scan was performed with T1W1 and T2W2, and the fat suppression BT side scan was performed in the sagittal position. The scanning layer thickness was 0.625 mm, the scanning interval was 0.5 mm, the pitch was 0.984 : 1, the matrix was 512 × 512, the voltage was 120 kV, and the current was 220–500 mA. Data measurement and image evaluation had to be included in the GE AW 4.2 workstation to be processed with Function tool II software. In addition, the ADC and FA were calculated according to the lesion status and the BT lesion diameter and number of lesions were recorded accordingly.

2.3. Criteria for Finding the Histological Grade of BT. The pathologically histological grade of BT was a key index for clinical BT treatment. The higher the grade, the greater the probability of tumor spread, the more difficult the treatment, and the greater the failure coefficient. At present, the histological grade was realized according to the three morphological characteristics of BT, including the formation of ducts, cell nuclear division, and the shape of the cell nucleus. The score for each morphological feature was 1–3 points, and the scores were accumulated to obtain three grades: grade I (3–5 points), grade II (6-7 points), and level III (8-9 points). The formation of ducts: 1 point was recorded for more than 75%; 2 points indicated 10%–75%; and 3 points indicated less than 10%. Cell nuclear division took 2 mm^2 as the basic unit: 1 point indicated 0–7 divisions; 2 points indicated 8–11 divisions; and 3 points suggested more than 12 divisions. The shape of the nucleus: 1 point was recorded for regular and normal shape; 2 points referred to enlargement, increased nuclear pores, and smaller nucleoli; and 3 points indicated shape change, increased nuclear pores, and large nucleoli.

2.4. Segmentation Procedures of CSD-MLS Algorithm. It was assumed that $\Pi \subset R^2$ represented the range of the image area, $a = (x, y) \in \Pi$ represented the point in the internal area of the image, and δ_j: $\Pi \longrightarrow R\,(j = 1, 2, 3)$ represented the level set function at II; $\{a\colon \delta_j(a) < 0\}$ referred to the target area; $\{a\colon \delta_j(a) > 0\}$ and $\{a\colon \delta_j(a) = 0\}$ referred to the range of the background area and the edge of the target area, respectively. Three level function sets $\delta_1(a)$, $\delta_2(a)$, and $\delta_3(a)$ represented the internal boundary of the breast, external boundary of the breast, and boundary of the tumor, respectively, as shown in Figure 1, which divided the entire area into 3 parts: the area Π_1 with normal breast tissue, the area Π_2 with BT tissue, and background area Π_3.

In the algorithm, the definitions of a large number of functions refer to the integrals in the corresponding area, such as the integral form being similar to $\int_{\Pi_i} g(a)da$. In this study, the integration ranges corresponding to different

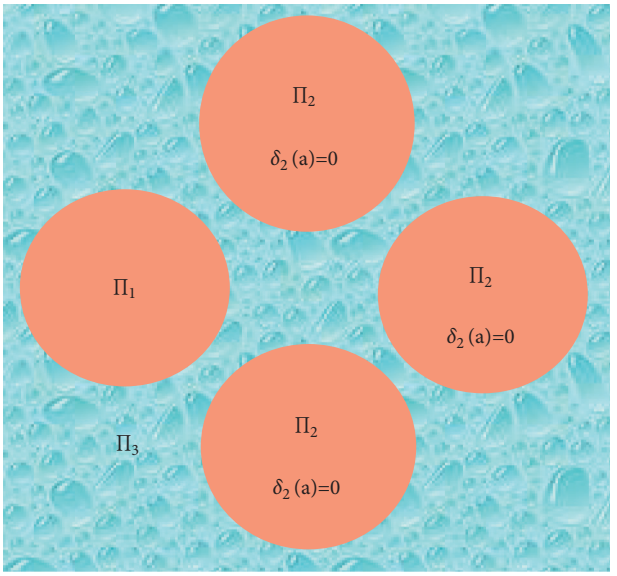

Figure 1: Level sets of the target range.

functions were expressed by the following equations for the areas in Figure 1:

$$\begin{aligned} N_1(a) &= 1 - R(\delta_1(a)), \quad a \in \Pi_1, \\ N_2(a) &= R(\delta_1(a))R(\delta_3(a)) - R(\delta_1(a))R(\delta_2(a))R(\delta_3(a)), \quad a \in \Pi_2, \\ N_3(a) &= R(\delta_1(a)) + R(\delta_1(a))R(\delta_2(a))R(\delta_3(a)) - R(\delta_1(a))[R(\delta_2(a)) + R(\delta_3(a))], \quad a \in \Pi_3. \end{aligned} \tag{1}$$

In the previous three equations, $R(m)$ represented a step function, whose derivative at $m=0$ was positive infinity, so $R_\psi(m)$ was used instead of $R(m)$ for the calculation, as follows:

$$R_\psi(x) = \frac{1}{2}\left[1 + \frac{1}{\pi}\arctan\left(\frac{x}{\psi}\right)\right]. \tag{2}$$

In (2), ψ was the scale parameter, which directly determined the derivative value of $R_\psi(m)$ at $m=0$. Through the above calculation of the inclusive number, the function $\int_{\Pi_i} g(a)\mathrm{d}a$ on $\Pi_i(1,2,3)$ can be replaced by $\int_{\Pi_i} g(a)N_i(a)\mathrm{d}a$.

The energy function of CSD-MLS met the following equations:

$$\begin{aligned} C(\delta_1(a), \delta_2(a)) &= C_c(\delta_1(a)) + C_q(\delta_2(a)) \\ C(\delta_3(a), t_p, t_q) &= C_p(\delta_1(a), \delta_2(a), \delta_3(a), t_p, t_q). \end{aligned} \tag{3}$$

In equation (3), C_c represented the energy value of the segmented BT area, C_p and C_q represented the energy values of the internal and external breast tissues, respectively, t_p referred to the gray value of the BT area, and t_q indicated the gray value of the normal breast tissue. The circle penalty item could be expressed as follows:

$$S(\delta(a)) = \int_\Pi (\delta(a) - \delta_s(a))^2 \mathrm{d}a. \tag{4}$$

In (4), $\delta_s(a)$ was the distance function. $S(\delta(a))$ was the minimum value when $\delta(a) = \delta_s(a)$. $\delta_1(a)$ was adopted to replace $\delta(a)$, and then, the energy value for segmenting the breast tissue could be calculated with the following equation:

$$\begin{aligned} C_c(\delta_1(a)) = \xi_c \int_\Pi f\theta(\delta_1(a))|\nabla\delta_1(a)|\mathrm{d}a \\ + \alpha_c \int_{\Pi_1} f\,\mathrm{d}a + \varphi_c B(\delta_1(a)). \end{aligned} \tag{5}$$

Here, ξ_c was the constant term, α_c was referred to as the spherical force coefficient, φ_c was the circle-dependent item, and f was the edge termination function, which could be defined as

$$f = 1/\left(1 + |\nabla F * J|^2\right). \tag{6}$$

In (6), F was the Gaussian filter, $|\nabla F * J|$ represented the strength of the graphic information, and the target boundary value of f at this time was the smallest. The Dirac function was a generalized function, which could be expressed as follows:

$$\phi_\psi(x) = \psi/\pi\left(\psi^2 + m^2\right). \tag{7}$$

Here, $\phi(x)$ represented the Dirac function and ψ referred to the scale parameter. In the iterative process, the position of the balloon force changed with the demonstration curve. The evolution equation was written as follows:

$$\mu(a) = \left[\frac{(\delta_1(a) - \sigma)}{b}\right]^{1/3}. \tag{8}$$

In (8), σ represented a fixed distance and b represented a buffer distance. α_c in equation (5) was replaced with $\mu(a)$, and then, the definition of energy function C_v could be obtained:

$$C_v(\delta_2(a)) = \vartheta_v C(\delta_1(a)) + \xi_v \int_{\Pi} f\theta(\delta_2(a)) \cdot \left|\nabla\delta_2(a)\right| \mathrm{d}a \quad quad + \mu(a) \int_{\Pi} G(-\delta_2(a)) \mathrm{d}a. \tag{9}$$

Here, the first, second, and third terms represented the circle-dependent term, the length term, and the balloon force term, respectively. ϑ_v and ξ_v referred to the coefficients of the circle-dependent term and the length term, respectively. If $\mu(a)$ was a positive number, it meant contraction, and if $\mu(a)$ was a negative number, it suggested expansion. The energy was minimized, and then $C_p(\delta_1(a), \delta_2(a), \delta_3(a), t_p, t_q)$ could be obtained based on equation (3). If $\partial C/\partial t_p = 0$ and $\partial C/\partial t_q = 0$ were true, the minimum value could be obtained. The specific equations are as follows:

$$t_p = \frac{\int JN_3 \mathrm{d}a}{\int N_3 \mathrm{d}a}, \qquad t_q = \frac{\int JN_2 \mathrm{d}a}{\int N_2 \mathrm{d}a}. \tag{10}$$

$\delta_3(a)$ was updated with the following equation:

$$\frac{\partial\delta_2}{\partial s} = \mu_\psi(\delta_3(a)) G_\psi(\delta_1(a)) \left(1 - G_\psi(\delta_1(a))\right) \cdot \left[\xi_p \left(J - t_p\right)^2 - \xi_q \left(J - t_q\right)^2\right]. \tag{11}$$

In (11), $\delta_1(a)$, $\delta_2(a)$, t_p, and t_q were the fixed variables.

2.5. Statistical Methods. The data processing in this study was analyzed by SPSS19.0 version statistical software. The measurement data were expressed as mean ± standard deviation ($\bar{x} \pm s$), and the count data were indicated as percentage. The one-way analysis of variance was employed to compare the lesion diameter, number of lesions, FA value, and ADC value of patients with grade I, grade II, and grade III. The difference was statistically significant at $P < 0.05$.

3. Results

3.1. Analysis on Segmentation Effects of Two Algorithms. The segmentation results of the CSD-MLS algorithm proposed were compared with those of the Live-Wire algorithm, and a histogram of the average of the Dice correlation coefficients of the two was drawn accordingly. Dice value represented the overlap between the segmentation standard and the actual segmentation result. The larger the Dice value, the better the segmentation. There was a horizontal line inside the rectangle, representing the average value of the Dice coefficient. The upper horizontal line on the rectangle referred to the maximum value, and the lower horizontal line represented the minimum value. 80% of the Dice value was distributed inside the rectangle. The average value of the Dice of the CSD-MLS algorithm was 0.75, and the average value of the Live-Wire algorithm was 0.62 (as shown in Figure 2), so the difference was statistically significant ($P < 0.05$). The distance between the maximum value and the minimum value was the smallest, indicating that the segmentation of this research algorithm was more accurate with good stability.

3.2. Imaging Characteristics of BT. BT tissue showed patchy low signal on T1WI and high signal on T2WI, with uneven signal intensity, blurred and irregular edges, star-shaped or burr-shaped masses, oedematous and thickened skin, and silt-like calcification, accompanied by axillary lymphadenopathy, nipple depression, and breast collapse on the affected side. The enhanced MRI examination showed mild to moderate enhancement and mainly delayed enhancement. Figure 3 shows a case of breast cancer in a female (47 years old). In MRI, the breast abscess showed low signal on T1WI and medium or high signal on T2WI, with uneven spot-like enhancement of breast parenchyma, clear boundary or part of the boundary, and a thick wall; the inflow and outflow curve after enhancement showed fast in and out (as shown in Figure 3). Figure 4 shows a female breast cancer case (54 years old). The upper quadrant of the left breast had an irregular shape with burrs on the edge. After the enhanced scan, it showed uneven and obvious enhancement. The front and lower parts of the lump extended to the level of the nipple with several small bumps (as shown in Figure 4). The lesion was tumor-like with mixed signals, showing the intensity of glandular and fat signals, growing around the large breast ducts, enhanced unevenly, and showing an outflow curve, with a thick blood vessel shadow, a slightly sunken left nipple, and no enlarged lymph nodes.

3.3. Histological Type of BT. In this study, there were a total of 293 lesions, all of which were in women, including 102 benign lesions and 191 malignant lesions. The pathological types of different benign lesions and the number of lesions were different. Compared with adenoma, the number of lesions of hamartoma and fibroma was less statistically

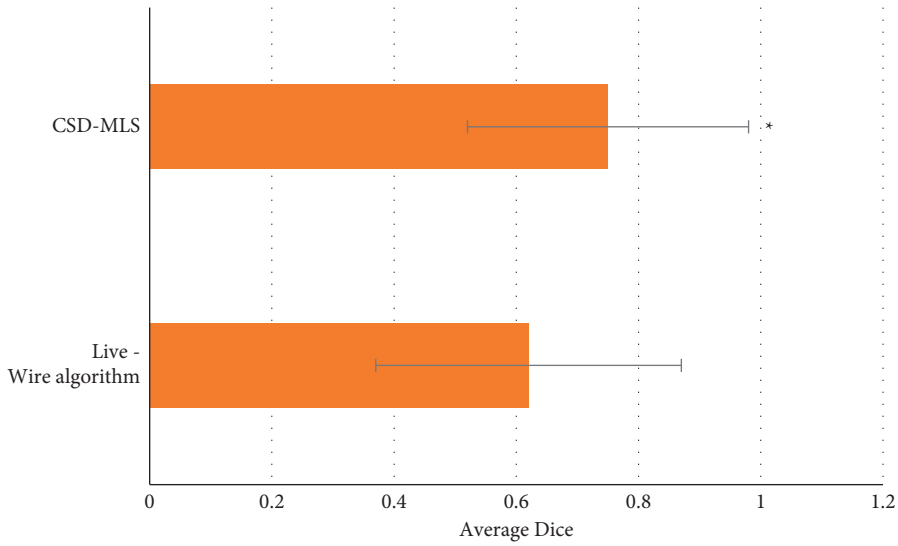

Figure 2: Comparison of average values of the Dice coefficient of two algorithms. *Note.* *Obvious differences in contrast to the Live-Wire algorithm ((P) < 0.05).

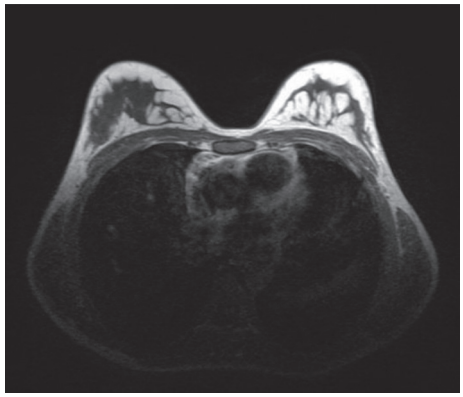

Figure 3: Enhanced edge.

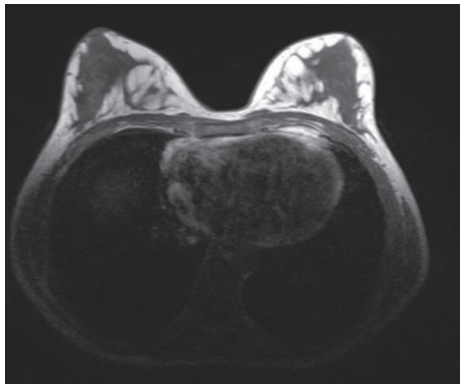

Figure 4: Blurs.

($P < 0.05$) (as illustrated in Figure 5). The pathological types and the number of lesions of the malignant lesions were also different. Compared with myxoma, the number of lymphoma and hemangiosarcoma was much less ($P < 0.05$) (as shown in Figure 6).

3.4. Histological Grade of BT. The patients in this study were subjected to prediction of histological grade of BT. It was found there were 38 patients with grade I, 152 patients with grade II, and 103 patients with grade III. Compared with the number of patients with grade II, the number of patients with grade I and grade III was greatly reduced with an observable difference ($P < 0.05$); the number of patients with grade I was much less in contrast to the number of patients with grade III with a huge difference ($P < 0.05$) (as shown in Figure 7).

3.5. Comparison of Lesion Sizes with Different Histological Grades of BT. The histological grade of BT had a reliable correlation with the lesion size instead of other imaging features. The measurement of the diameter of the lesion of different histological grades found that compared with the lesion diameter of grades I and III, that in grade II was concentrated in 1.5–2.5 cm ($P < 0.05$) and the lesion diameter of grade III was concentrated in 2.5–3.5 cm which was visibly different from that of grades I and II ($P < 0.05$), as shown in Figure 8.

3.6. Comparison of FA Values with Different Histological Grades of BT. The FA values of patients with different histological grades were compared, and the results are shown in Figure 9. It disclosed that the FA value of patients with grade I was much higher than that of patients with grade II ($P < 0.05$) and the FA values of patients with grade I and grade II were much higher in contrast to those of grade III disease, with a considerable difference ($P < 0.05$).

3.7. Comparison of ADC Values with Different Histological Grades of BT. The ADC values were compared for patients with different histological grades, and the results are shown in Figure 10. It indicates that the ADC value of patients with grade I was much lower than that of patients with grade II

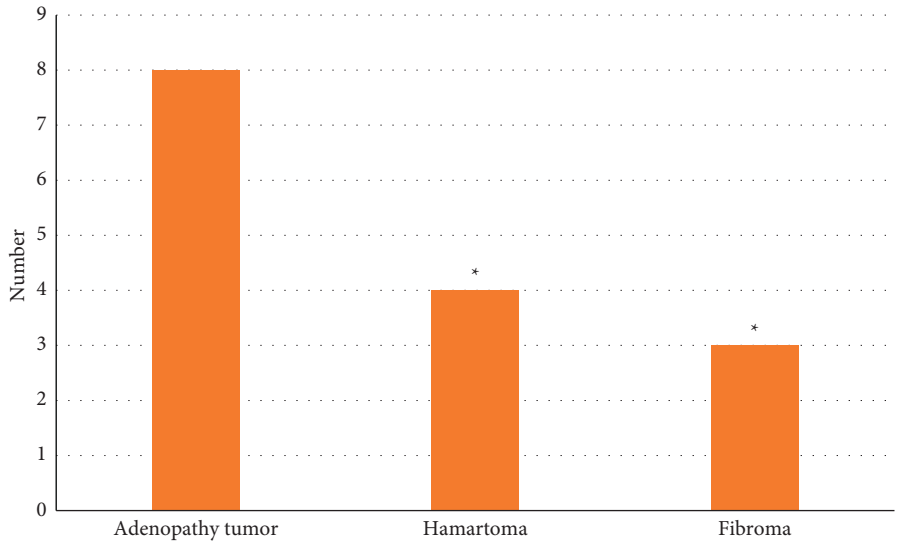

Figure 5: Distribution of benign lesions in BT. *Note.* *The difference was obvious in contrast to the adenoma ($P < 0.05$).

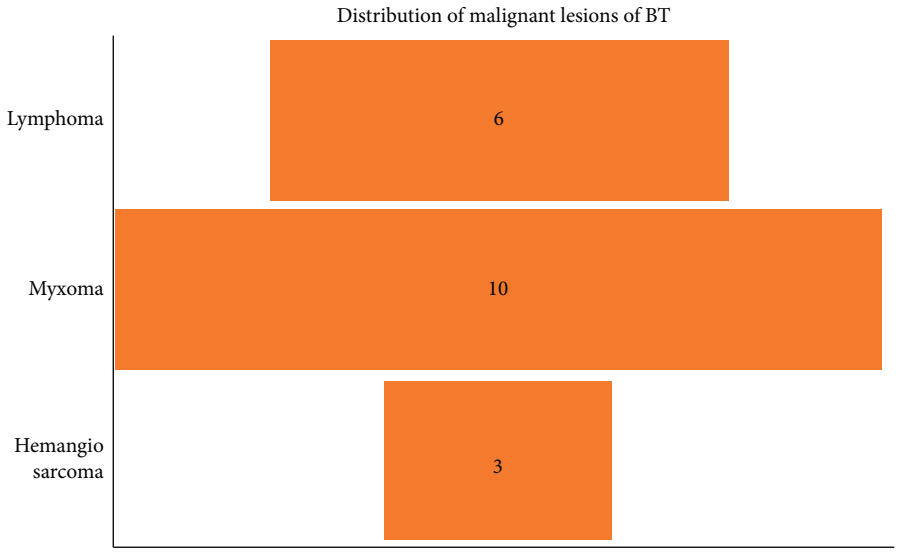

Figure 6: Distribution of malignant lesions of BT. *Note.* *The difference was obvious in contrast to the myxoma ($P < 0.05$).

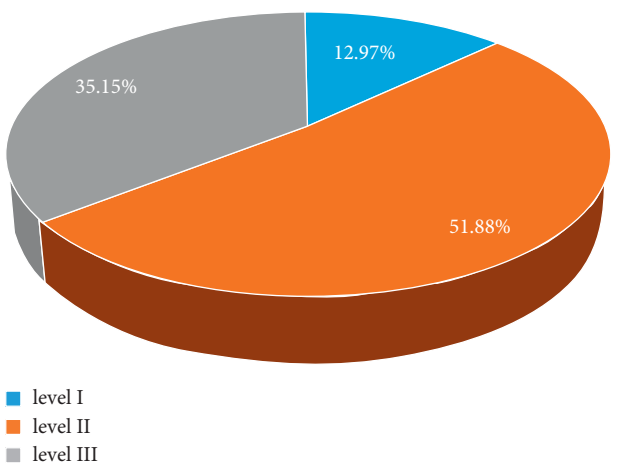

Figure 7: Proportions of different histological grades of BT.

($P < 0.05$) and the ADC values of patients with grade I and grade II were much lower than those of patients with grade III with statistical significance ($P < 0.05$).

4. Discussion

BT is the most common malignant tumor that occurs in women, and its incidence has been increasing in recent years. The annual incidence of BT in China has increased by about 4%, especially in large cities, where BT has consistently ranked among the top two in female cancer [13]. For a long time, national and international scholars have spent a lot of time studying the pathogenic factors of BT, but so far, no research has clearly pointed out its independent risk factors [14]. MRI images have a good resolution effect on tissues and low radiation. Compared with CT and ultrasound, MRI images show obvious advantages in the examination of

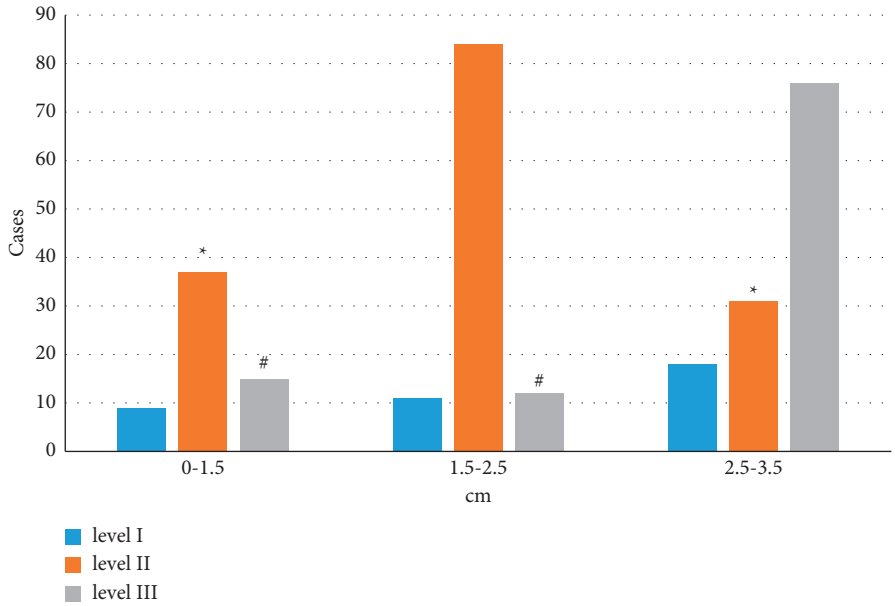

Figure 8: Lesion sizes of different histological grades of BT. *Note.* $^{*,\#}P < 0.05$ in contrast to the lesion diameter of 1.5–2.5 cm and 2.5–3.5 cm, respectively.

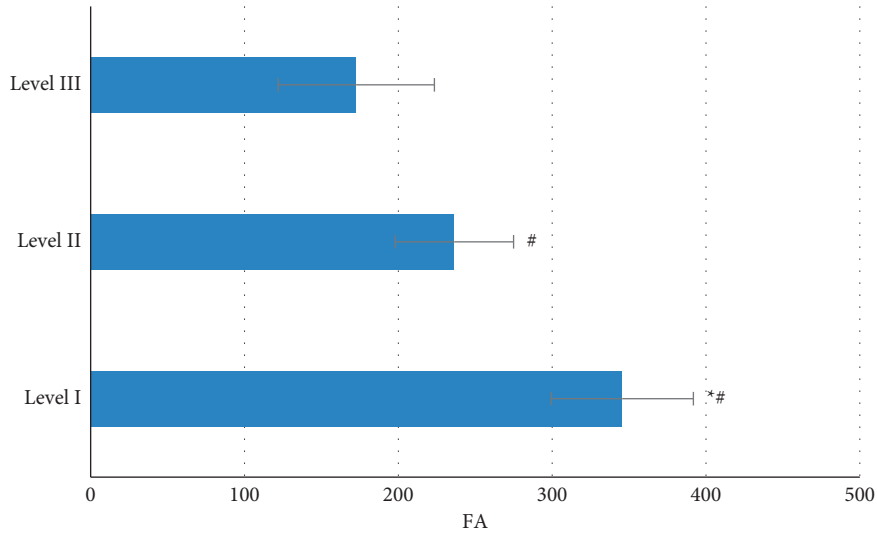

Figure 9: Comparison of FA values of different histological grades of BT. *Note.* $^{*,\#}P < 0.05$ in contrast to grade II and grade III, respectively.

breast parts. Especially after the addition of modified breast coils and the use of contrast agents, MRI images used to evaluate the BT have made great progress by leaps and bounds [15]. The Washington Medical Center (WMC) pointed out at an annual meeting that MRI evaluation was the best method of pathological examination of female BT patients [16]. The CSD-MLS algorithm proposed in this study was compared with the Live-Wire algorithm. The average value of the Dice coefficient of the CSD-MLS and Live-Wire algorithms was 0.75 and 0.62, respectively ($P < 0.05$), with the minimum distance between the maximum value and the minimum value, indicating that the segmentation of the proposed algorithm was more accurate with good stability. Some studies have applied computer semiautomatic segmentation algorithms to the diagnosis and treatment of glioma, which overcomes the defect that glioma images are complex and changeable and it is difficult to accurately extract essential features, which greatly improves the accuracy of MRI diagnosis of the disease. Such a conclusion is more consistent with the results of this study [17].

Kim et al. (2018) [18] once reported that the MRI image of a breast abscess showed high signal on T2WI with smooth and flat surrounding tissue and a liquid state inside. The MRI image of breast abscess in this study showed clear boundaries with medium or high signal on T2WI, which was consistent with the above research results. Pinker et al. (2018) [19] pointed out that ADC value was one of the most important indicators reflecting the characteristics of dispersion, and it could reflect the density and growth of BT

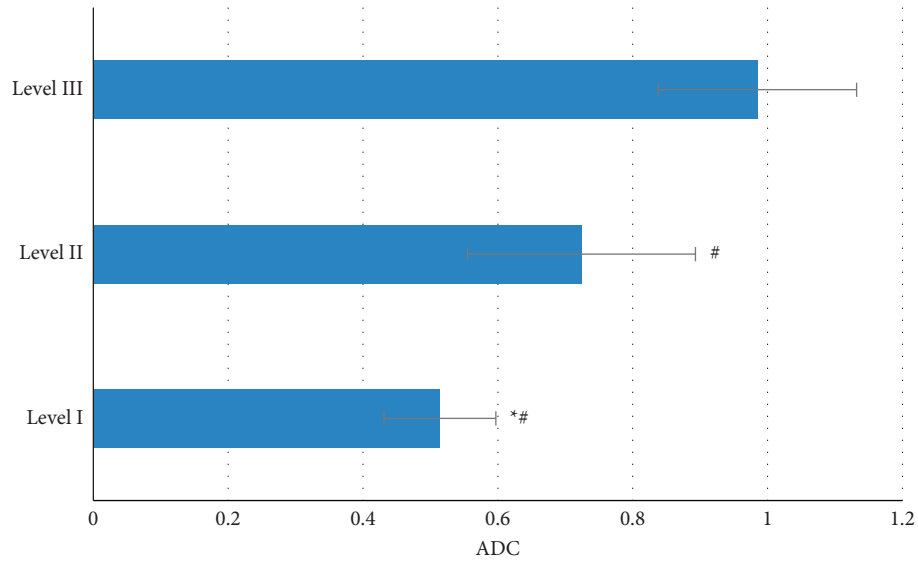

Figure 10: Comparison of ADC values of different histological grades of BT. *Note.* $^{*,\ \#}P < 0.05$ in contrast to grade II and grade III, respectively.

tissue, which was a very important criterion for tumor diagnosis. Farrokh et al. (2019) [20] pointed out that the histological grade of BT was correlated with the size of the lesion. It was found in this study that the lesion diameters of grade II and grade III were concentrated at 1.5–2.5 cm and 2.5–3.5 cm, respectively ($P < 0.05$), indicating that there was indeed a certain correlation. Wien beck et al. (2019) [21] believed that the ADC value was positively correlated with the internal structure of BT cells and the more the types of cell tissues, the greater the ADC value. In this study, the ADC values of patients with grades I and II were lower than those of patients with grade III. In addition, a comparison of the FA values of patients with different tissue grades showed that the FA values of grade I patients were significantly higher than those of grade II patients ($P < 0.05$) and the FA values of grade I and II patients were significantly higher than those of grade III patients ($P < 0.05$). The pathological type and number of different benign lesions were also different. Compared with adenomas, ham tumors and fibroids had fewer lesions, showing statistically significance ($P < 0.05$). In addition, the pathological type and number of malignant lesions were also different. Compared with fibroids, the number of lymphomas and angiosarcomas was significantly reduced ($P < 0.05$). It might be that as the disease continued to develop, the metabolism of BT tissue cells became stronger and stronger, which increased the density of cells and narrowed the gap among cells, so that the range of water molecules was restricted.

5. Conclusion

The CSD-MLS algorithm proposed in this study was compared with the Live-Wire algorithm in terms of segmentation results, and it was applied to MRI images for prediction of BT histological grade. The results revealed that the segmentation of the proposed algorithm in this study was accurate and had good stability. The histological grade of BT had a correlation with lesion size, number of lesions, ADC value, and FA value. The shortcoming of this study was that the sample size of BT tissue was limited, so the statistical results of pathology grades I, II, and III were not exact enough. Later, the sample size had to be expanded and further researched. In short, the histological grade of BT could effectively assess the severity of BT and provide a reliable reference for the advancement of clinical diseases.

Data Availability

The data used to support the findings of this study are available from the corresponding author upon request.

Conflicts of Interest

The authors declare no conflicts of interest.

Authors' Contributions

Jiyuan Wang and Yanling Zhou contributed equally to this work.

References

[1] A. Menta, T. M. Fouad, A. Lucci et al., "Inflammatory breast cancer: what to know about this unique, aggressive breast cancer," *Surgical Clinics of North America*, vol. 98, no. 4, pp. 787–800, 2018.

[2] X. Li, J. Yang, L. Peng et al., "Triple-negative breast cancer has worse overall survival and cause-specific survival than non-triple-negative breast cancer," *Breast Cancer Research and Treatment*, vol. 161, no. 2, pp. 279–287, 2017.

[3] M. Thomas, E. D. Kelly, J. Abraham, and M. Kruse, "Invasive lobular breast cancer: a review of pathogenesis, diagnosis, management, and future directions of early stage disease," *Seminars in Oncology*, vol. 46, no. 2, pp. 121–132, 2019.

[4] S. Blissett, M. Chetrit, B. Kovacina, V. Mardigyan, and J. Afilalo, "Performing cardiac magnetic resonance imaging in

patients with cardiac implantable electronic devices: a contemporary review," *Canadian Journal of Cardiology*, vol. 34, no. 12, pp. 1682–1686, 2018.

[5] M. A. Marino, C. C. Riedl, M. Bernathova et al., "Imaging phenotypes in women at high risk for breast cancer on mammography, ultrasound, and magnetic resonance imaging using the fifth edition of the breast imaging reporting and data system," *European Journal of Radiology*, vol. 106, pp. 150–159, 2018.

[6] Y. Zhai, J. Liu, J. Zeng et al., "Deep convolutional neural network for facial expression recognition," *Lecture Notes in Computer Science*, vol. 106666, pp. 211–223, 2017.

[7] P. Naveen and P. Sivakumar, "Adaptive morphological and bilateral filtering with ensemble convolutional neural network for pose-invariant face recognition," *Journal of Ambient Intelligence and Humanized Computing*, vol. 12, no. 11, pp. 10023–10033, 2021.

[8] K. Zheng, Z. Wen, and D. Li, "The clinical diagnostic value of lumbar intervertebral disc herniation based on MRI images," *Journal of healthcare engineering*, vol. 2021, Article ID 5594920, 2021.

[9] P. Padhye, A. Alam, S. Ghorai, S. Chattopadhyay, and P. Poddar, "Doxorubicin-conjugated β-NaYF4:Gd3+/Tb3+ multifunctional, phosphor nanorods: a multi-modal, luminescent, magnetic probe for simultaneous optical and magnetic resonance imaging and an excellent pH-triggered anticancer drug delivery nanovehicle," *Nanoscale*, vol. 7, no. 46, pp. 19501–19518, 2015.

[10] Y. Li, J. Zhao, Z. Lv, and J. Li, "Medical image fusion method by deep learning," *International Journal of Cognitive Computing in Engineering*, vol. 2, no. 6, pp. 21–29, 2021.

[11] J. Cheng, Y. Chen, Y. Yu, and B. Chiu, "Carotid plaque segmentation from three-dimensional ultrasound images by direct three-dimensional sparse field level-set optimization," *Computers in Biology and Medicine*, vol. 94, pp. 27–40, 2018.

[12] M. Latha and G. Kavitha, "Segmentation and texture analysis of structural biomarkers using neighborhood-clustering-based level set in MRI of the schizophrenic brain," *Magnetic Resonance Materials in Physics, Biology and Medicine*, vol. 31, no. 4, pp. 483–499, 2018.

[13] T. Li, C. Mello-Thoms, and P. C. Brennan, "Descriptive epidemiology of breast cancer in China: incidence, mortality, survival and prevalence," *Breast Cancer Research and Treatment*, vol. 159, no. 3, pp. 395–406, 2016.

[14] S. Schlesinger, D. S. M. Chan, S. Vingeliene et al., "Carbohydrates, glycemic index, glycemic load, and breast cancer risk: a systematic review and dose-response meta-analysis of prospective studies," *Nutrition Reviews*, vol. 75, no. 6, pp. 420–441, 2017.

[15] H. Kim, W. Park, S. S. Kim et al., "Outcome of breast-conserving treatment for axillary lymph node metastasis from occult breast cancer with negative breast MRI," *The Breast*, vol. 49, pp. 63–69, 2020.

[16] S. Al-Hattali, S. J. Vinnicombe, N. M. Gowdh et al., "Breast MRI and tumour biology predict axillary lymph node response to neoadjuvant chemotherapy for breast cancer," *Cancer Imaging*, vol. 19, no. 1, p. 91, 2019.

[17] P. Naveen, P. S. Babu, K. Chaitanya, and S. A. S. Basha, "Image enhancement in low-light conditions using volume-based subspace interpretation," *International Conference on Intelligent Computing and Control Systems*, vol. 2021, no. 5, pp. 766–771, 2021.

[18] K. W. Kim, C. M. Kuzmiak, Y. J. Kim, J. Y. Seo, H. K. Jung, and M.-S. Lee, "Diagnostic usefulness of combination of diff usion-weighted imaging and t2wi, including apparent diffusion coefficient in breast lesions: assessment of histologic grade," *Academic Radiology*, vol. 25, no. 5, pp. 643–652, 2018.

[19] K. Pinker, L. Moy, E. J. Sutton et al., "Diffusion-weighted imaging with apparent diffusion coefficient mapping for breast cancer detection as a stand-alone parameter: comparison with dynamic contrast-enhanced and multiparametric magnetic resonance imaging," *Investigative Radiology*, vol. 53, no. 10, pp. 587–595, 2018.

[20] A. Farrokh, L. Treu, R. Ohlinger, C Flieger, N Maass, and F. K Schäfer, "A prospective two center study comparing breast cancer lesion size defined by 2D shear wave elastography, b-mode ultrasound, and mammography with the histopathological size," *Ultraschall in der Medizin*, vol. 40, no. 2, pp. 212–220, 2019, English.

[21] S. Wienbeck, J. Uhlig, U. Fischer et al., "Breast lesion size assessment in mastectomy specimens: correlation of cone-beam breast-CT, digital breast tomosynthesis and full-field digital mammography with histopathology," *Medicine*, vol. 98, no. 37, Article ID e17082, 2019.